# Highlights

**A thick cellular structural adhesive : Identification of its behavior under shear loading**

Maxime Wetta, Jean-Benoit Kopp, Louise Le Barbenchon, Philippe Viot

- Core-skin effect highlighted in the microstructure of a thick cellular structural adhesive (TCSA);
- Evaluation of the shear properties of a TCSA using the Arcan test and digital image correlation;
- The macroscopic shear modulus and the maximum shear strain at failure of TCSA are mainly driven by macroscopic density which is not the case for the maximum shear stress at failure.

# A thick cellular structural adhesive : Identification of its behavior under shear loading

Maxime Wetta[a], Jean-Benoit Kopp[a], Louise Le Barbenchon[b], Philippe Viot[a]

[a] *Arts et Metiers Institute of Technology, CNRS, I2M Bordeaux, Esplanade des arts et metiers, Talence, F-33400, France*

[b] *CNRS, Arts et Metiers Institute of Technology, I2M Bordeaux, Esplanade des arts et metiers, Talence, F-33400, France*

**Abstract**

This study focuses on the link between the microstructure and the mechanical behavior under shear loading of a thick cellular structural adhesive (TCSA). X-ray microtomography and image post-processing were first used to perform 3D-quantitative microstructure analysis. The cells morphometric parameters and their orientations were studied. The foaming process boundary conditions seems to create local density gradients changing the cells dimensions and shape. The cells are more spherical in the core of the material whereas being more ellipsoidal close to the upper and lower faces of the samples creating a skin layer. The effect on the strain field of this skin layer has then been highlighted . Secondly, a shear test method using an Arcan set-up coupled with digital image correlation was used and allowed to observe the mechanical behavior of the material under shear loadings. Instead of the material being cellular and heterogenous, it has been found that the strain field can be considered homogeneous at macroscopic scale to extract the properties on a homogeneous equivalent material. Shear test on samples with different

densities were performed. Using the relation developed by Gibson and Ashby linking the shear modulus to the density squared is a first approximation, at this scale, to predict and describe the mechanical behavior under shear loading.

*Keywords:* Foam, Epoxy adhesive, Arcan shear test, X-Ray Tomography, Microstructure

## 1. Introduction

Structural bonding is a stiffness reinforcement technique that has been developing over the last 50 years. There are other joining methods such as riveting, welding, and bolding but these techniques create stress concentrations as well as oxidation and weight problems. Therefore, bonding is very popular in a large number of industrial sectors that use metals and composites: the transportation industry (cars, boats, airplanes, trains), civil engineering (solar panels, bridges) or medical prosthesis. For structural adhesives, the base material is synthetic polymers like epoxy (thermosetting) or acrylic (thermoplastic) [1] resins.

During their lifetime, structural bondings may endure all types of loadings. These materials are usually strongest in shear and compression but relatively weak under peel and cleavage. The design of the joints should take this into account to reach the highest resistance [2]. Manufacturers and suppliers consider that the main role of the adhesive is to transfer load from one adherend to another through a shearing action [1]. Thus, the mechanical characteristics of the material under shear loading are very important for design calculations.

Several shear tests are used to characterize adhesives. The most commonly used in the industry are standardized as Single Lap [3] or TAST for thicker adhesives [4]. There is also the Scarf test [5], which is not standardized. However, the Arcan test, initially developed by the researcher of the same name [6], has been shown to create uniform plane-stress states [7, 8] in adhesive bonds. Since then, this solution has been used with digital image correlation (DIC) to characterize the elastic shear moduli of orthotropic materials [9, 10], to test adhesively-bonded assemblies for the automotive industry [11].

Several studies have shown that the properties of conventional adhesive joints tend to decrease with increasing joint thickness. Sources agree that the thickness impacts the stress field due to parasitic moments and stress concentration related to the structure [12, 13, 14]. It is then necessary to also take into account bulk properties rather than just joint properties [15, 16]. But most studies on structural adhesives involve bond lines that are between 0.1 and 2-3 mm thick. Studies on thicker adhesives (5 to 10 mm) are limited, recent and focused to specific fields such as the marine and wind industries [17, 16, 18].

To link part of structures with large gaps and complex geometry between parts while limiting the final weight, expanded structural adhesives have been developed in the industry. By using cellular-structured composite materials or high performance bonding resins like epoxy, the mechanical characteristics of the structure can be improved with a reduced weight [19, 20, 21]. However, the knowledge on these cellular-structured adhesives in the literature is poor and the influence of the manufacturing process on their mechanical properties

little understood. The state of industrial knowledge in the sector indicates that these materials have a cellular material behavior at the macroscopic level. However, in some cases, such as interface fractures, the behavior would seem to be closer to a classical adhesive. It is therefore necessary to explore knowledge from both adhesives and cellular materials fields of study.

Historically, many studies have focused on metallic foams which have very good mechanical properties [22, 23]. But in the last three decades the use of polymeric foams has increased significantly due to the improved strength of the materials coupled with their intrinsic low density.

Studies of polymeric cellular materials began really in the 1980s with, for example Siegmann et al. [24] predicting elastic properties of polyurethane foams using the Kerner equations [25]. Gibson and Ashby [26] provided then description of the relationship between the cell structure morphology and the governing parameters of the mechanical behavior. Fabrice Saint-Michel et al. [27] verified the effect of the density on the mechanical properties of high density polyurethane foams comparing Gibson and Ashby [26] and Christensen and Lo [28] models. The macroscopic response of foams under high compression rates have also been shown to be linked to microstructure [29, 30, 31] as well as its fracture properties [32].

The foaming process for the cellular material creation is important to understand. Indeed, it is known in the literature, as for example for injection process, that anisotropy can appear in cellular structures due to the nucleation [21, 33]. Gomez-Monterde et al. [34] have shown that the mechanical properties can be modified because of this phenomenon. The anisotropic behavior of the polymer increased due to the cell elongation caused by the

injection flow.

Few studies exist in the literature to investigate in detail the behavior under shear stress of cellular materials. The shear strain of cellular materials have recently been locally analyze with DIC and Arcan fixtures [35, 36]. The study of the material remains however often external and not volumetric.

The objective of this paper is a description and an analysis of the link between cellular microstructure of a thick cellular structural adhesive (TCSA) and its behavior under shear loading. The morphology heterogeneity in the material due to the process is first studied. A 3D-quantitative microstructure analysis is made possible thanks to X-ray microtomography and image post-processing. Then, a method using the Arcan test coupled with DIC is developed to characterize the mechanical behavior of the TCSA material under shear loading. The study will focus on samples of two different densities and then two different microstructures.

## 2. Material and Methods

In this section the studied material will be described. Then the X-Ray tomography images acquisition and their treatment are presented before a mechanical testing method using the Arcan shear test and DIC.

### *2.1. Thick cellular-structured adhesive (TCSA)*

Epoxy resin is a thermosetting polymer commonly used for strong adhesion. It expands when cured at high temperature via the incorporation of a blowing agent reacting while the cross-linking of the resin is occurring. The resulting material is a thick adhesive with a cellular microstructure.

Material samples of dimensions $\approx 50 \times 30 \times 4\ mm^3$ are cut from an A5-sized injected plate before being expanded using the assembly presented in the Figure 1. This assembly consists of two rigid metallic plates spaced by hollow shims of known thickness. Release paper is added between the plate and the material to prevent the adhesion of the material to the metal. The objective is first to control the density of the material by controlling the height of expansion. Samples with two different thicknesses $t$ were manufactured : $t = 5\ mm$ and $t = 7\ mm$. To describe cellular materials, the notion of relative density $\rho_r = \rho^*/\rho_s$ is commonly introduced. The density $\rho^*$ is that of the cellular material while $\rho_s$ is that of the same fully dense material. After expansion, samples with relative density $\rho_{r,high} = 0.49$ (for $t = 5\ mm$) and $\rho_{r,low} = 0.45$ ($t = 7\ mm$) are obtained. These macroscopic densities have been measured with laboratory density scales. By disregarding the adhesive function, one tries to determine only the volumetric properties of the material.

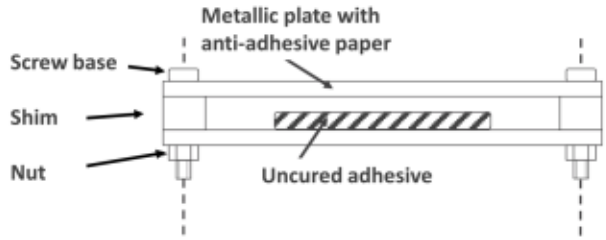


Figure 1: Set-up controlling the expansion height.

Two samples of the two different densities $\rho_r$ were cut with a band saw to obtain parallelepipeds of dimensions $\approx 45 \times 10 \times t\ mm^3$. They were then observed by X-ray tomography as explained in the section titled X-Ray

micro-tomography.

Parallelepipeds were cut out of the expanded material samples using a band saw. To achieve the desired dimensions of $40 \times 21 \times e\ mm^3$, a sander with a P120 grit disc was used (step 1 in Figure 2). They were then glued with a device to create the Arcan test samples. The steps (step 2 for gluing and 3 for verification) in Figure 2) are described in the section Arcan shear test - sample preparation.


Figure 2: Gluing protocol for Arcan samples with a set-up allowing parallelism.

### *2.2. X-Ray micro-tomography*

It is difficult to properly analyze the cellular materials structure with only 2D methods like light or scanning electron microscopy. Indeed, there is a loss of information into volume such as the coalescence of the cells. To eliminate this problem and observe in 3D, X-ray microtomography with a GE v|tome|x s tomograph available at Placamat Bordeaux was used. The general principle of the X-ray microtomography technique applied to the material science has already been described in an article by Maire et al. [37].

The resolution was 8.5 $\mu m/voxel$ for the low density sample and 10 $\mu m/voxel$ for the high density one. The first one having a smaller thickness, it was possible to obtain a slightly better resolution with the laboratory tomograph. However, this did not result in a better observation afterwards, the difference

being weak. Whatever the density, this technique is assured to have sufficient resolution regarding the size of the cells.

The 3D reconstruction of the samples and the quantitative analysis of the structural parameters of the material are performed using the Amira-Avizo software.

The study volume, also called volume of interest (VOI), is a prismatic sub-volume. It is in this VOI that the morphometric parameters are calculated. This sub-volume is chosen with dimensions slightly smaller than the sample to avoid edge effects due to sample preparation. For the low density sample, its dimensions are $9 \times 6 \times 10\ mm^3$. To keep the same width/height ratio, with the high density sample the dimensions of the VOI are $8.1 \times 4.3 \times 10\ mm^3$.

### *2.3. 3D Image analysis*

The images being originally in 16 bits were converted to 8 bits (see in Figure 3a). Due to the large difference between the linear attenuation coefficients of air and epoxy, the grey-level distribution of the images is almost bimodal. A threshold then allows the image to be binarized as needed (see in Figure 3b). The pixels have intensity values from 0 to 90 for the cells (the void) and from 90 to 255 for the polymeric phase.

The 3D segmentation method is divided into three main steps [38]. First, the distance map image of the cells is computed. The right markers are then selected by topographic conditions. Finally, the watershed method is constructed from these markers with the help of the distance function (see results in Figure 3c). Then, one can label and study the cells one by one (Figure 3d). It is possible to analyze separately the polymeric phase (in Figure 4a)) or the porosities (in Figure 4b)).

Studies on cork [39] and aluminum [40] foams highlight the difficulty of image segmentation on heterogeneous cellular materials. There is not yet a technique to quantify the accuracy of this method. Recently, deep learning was tested to improve these algorithms [41].

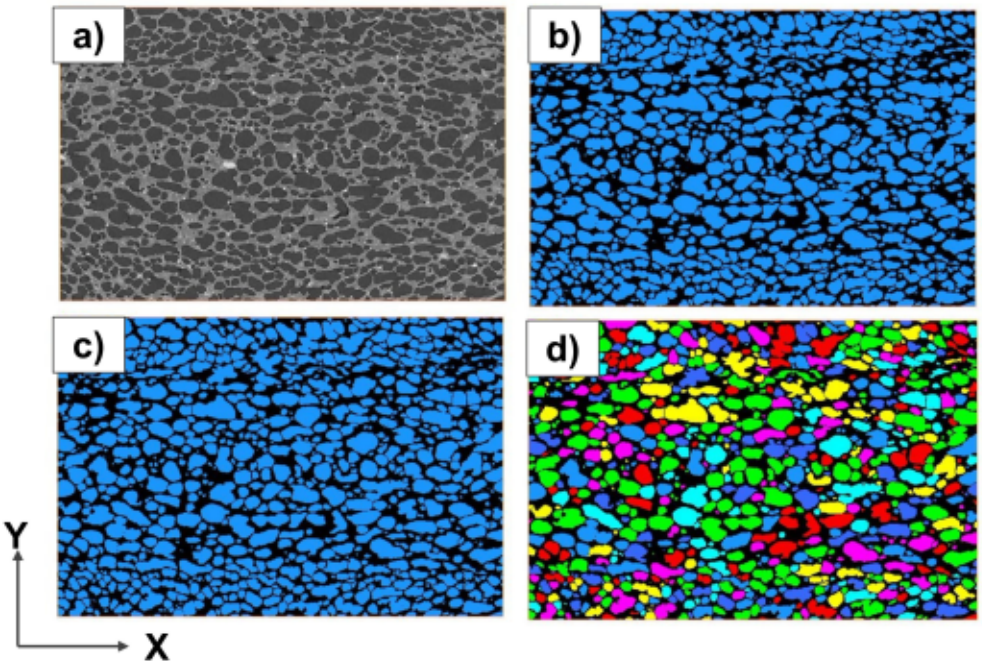


Figure 3: Image processing steps (a)-(d) for the 3D reconstruction of the cells.

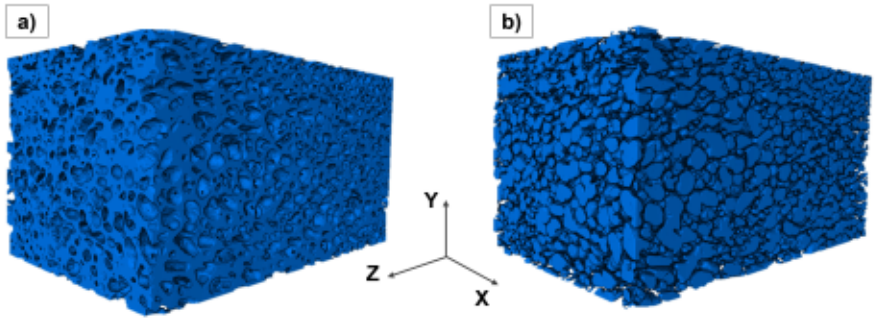


Figure 4: 3D reconstruction of the polymeric phase (a) and the porosities only (b). The represented volume size is $9 \times 6 \times 10\ mm^3$.

The considered parameters are the length, width, volume, orientation, anisotropy and sphericity of the cells.

The length and width of the cells are defined as the maximum and minimum values of the Feret diameters respectively. One recalls that the Feret diameter is a one-dimensional measurement to estimate the size of an object along a direction. For the analysis of a 3D particle, the object is projected in a 2D plane and the Feret diameter is the distance between two parallel tangent lines [42].

All cells with a volume smaller than $10^{-6}\ mm^3$ are removed. It is impossible with the available resolution to identify them. The classical spherical coordinate angles $\theta$ and $\phi$ are used for the cell orientations. The mathematical convention calling $\theta$ the azimuthal angle and $\phi$ the polar angle is used to to simplify software processing (see in Figure 5).

Sphericity $\psi$ measures how closely the shape of an object approaches a mathematically "perfect" sphere. It is calculated according to Eq. 1

$$\psi = \frac{\pi^{\frac{1}{3}}(6V_p)^{\frac{2}{3}}}{A_p}, \tag{1}$$

with $V_p$, the volume of the particle and $A_p$, the external surface area of the particle. The nearer to 1, the closer to a sphere.

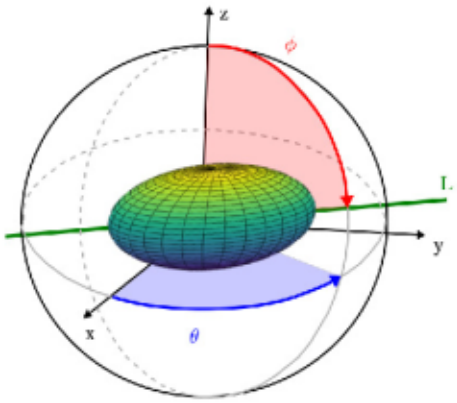


Figure 5: Orientation of the cells in a spherical coordinate system.

### *2.4. Arcan shear test - sample preparation*

The Arcan device consists of a bonded specimen clamped in two half disk shaped pieces. The Arcan adherends are manufactured from Aluminium 7075 T6 ($E = 72\,GPa$ and $\nu = 0.33$). The size of the bonding surface is $40{\times}21\ mm$ ($840\ mm^2$). The metallic adherends were cleaned with alcohol and acetone before being air dried. After setting and clamping the adherends, Loctite EA 9466 epoxy adhesive was applied. The material specimens were then placed on the adherends. The assembly was then put in place as shown in the step 2 in Figure 2. Large shims are used to control the adhesive thickness at 0.5mm on each side. Excess adhesive was directly removed.. This step was performed a second time after 45 min, as the glue was not yet fully cured.

The assembly was then left for at least 24 hours at room temperature before disassembly to ensure the glue cross-linking. The final result is shown in step 3 in Figure 2.

The tests were performed on 10 high density and 15 low density samples. The difference in macroscopic density between each sample for both sample types (high or low density) was equal or less than 0.01 $g/cm^3$

### *2.5. Test set-up and protocol*

The Arcan tests were performed with the help of a Zwick Z010 tensile machine as shown in Figures 6a and 6b. The force was measured with a 10 kN load cell. The crosshead was driven with a constant displacement speed of 0.5 mm/min. To limit the displacement uncertainty at the beginning of the test due to the gaps in the set-up, a preload of 50 N was systematically applied.

For image acquisition during the test, a Canon 800D camera with a macroscopic lens is used. Its resolution is $4000 \times 6000$ pixels. The camera is mounted on a tripod and the focus is adjusted manually. The LED light allows to adjust the brightness without increasing the temperature of the sample (checked with a laser thermometer). A signal is sent by the computer to acquire pictures at a sampling rate of 0.33 $Hz$. To be able to use the image correlation tools, a white and black paint speckle was sprayed on the material as well as on the metallic adherends. Both the adherends and the sample were placed in the field of view.

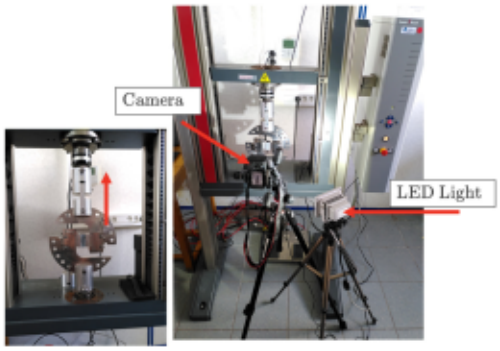


(a) Arcan set-up.

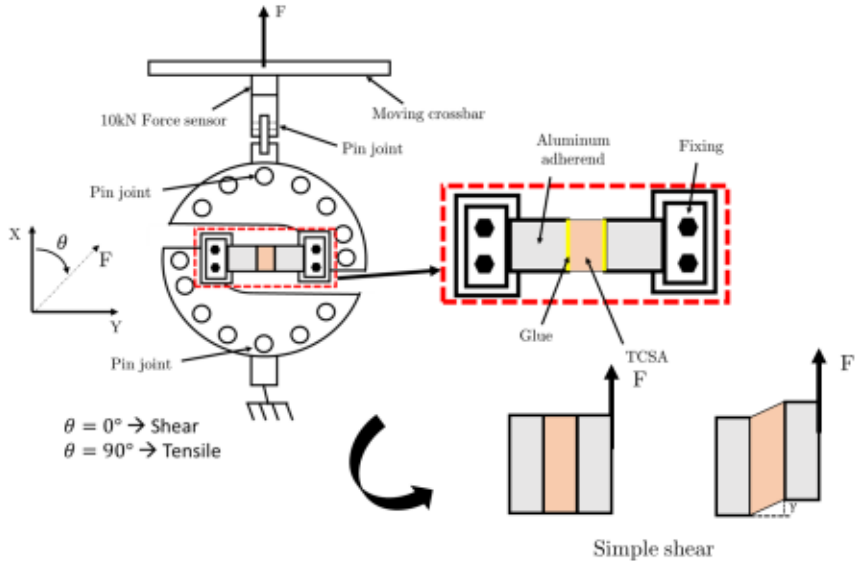


(b) Arcan schematic drawing.

Figure 6: Arcan set-up and schematic drawing.

### *2.6. Digital image correlation (DIC)*

It is therefore necessary to take into account local behavior of the materials under loadings. Digital image correlation (DIC) is a powerful tool to analyze locally small displacements of materials [43]. This method has already been used coupled with the Arcan test to characterize the shear be-

havior of heterogeneous materials such as wood [10] or bones [9] under shear loading. Studies have also shown the usefulness of this technique to study the local behavior of foams under high speed compression [44],[45].

In the Arcan test, the displacements can be described by a 2D analysis. For the DIC processing, the Vic2D software from Correlated Solutions is used. The data are then exported and processed using GNU Octave and Matlab.

On each image a calculation area called "Area of interest" (AOI) is defined. These areas are divided into "subsets" which each has their own gray scale spectrum. The size of these subsets is chosen to obtain a good estimation of the displacement field. At least 20 subsets in length and 5 in height of the sample were chosen. The post-processing consists in calculating the Lagrange deformation tensors $E$ from the displacement field. From these it extracts the engineer's deformations and more particularly the shear strain, $\gamma$,

$$\gamma = \sin^{-1}\left(\frac{2E_{xy}}{(1+2E_{xx})(1+2E_{yy})}\right), \tag{2}$$

knowing that $x$ is defined according to the length of the sample and $y$ according to its height (as seen in Figure 6). The evolution of the average $\gamma$ angle during the test is then exported.

The shear modulus, the ultimate shear strength and the maximum shear strain of the material were calculated. To obtain the stresses the force acquired by the machine was divided by the initial sheared surface, $S_0$. This surface was considered to be the cross-section of an equivalent homogeneous material of the same dimension. Displacements and shear strain are obtained

by DIC measurement.

## 3. Results and discussion

**Quantitative morphometric data extraction using 2D slices is not suitable. Indeed, a large part of the information is only accessible from volumetric data. The former will therefore allow a qualitative analysis of the phenomenon while all the quantitative data will be extracted from the volume reconstruction analysis explained in section 2.3.**

### *3.1. Microtomography results*

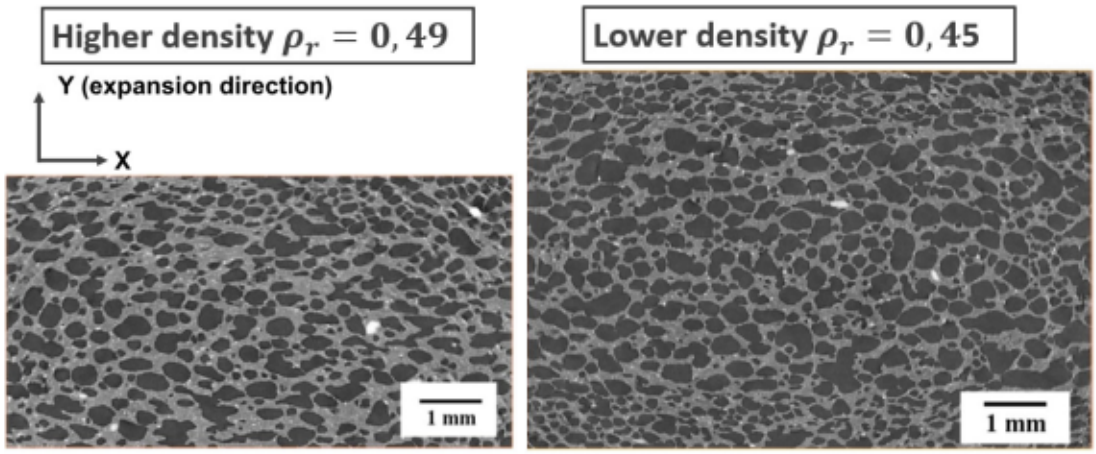


Figure 7: X-Ray Tomography slices for both high and small densities samples.

After sorting the data to remove the noise one studies about 20000 cells for the low density sample and 10000 for the high density sample. The volume ratio being only 1.55 it seems that there are less cells in the high density sample. For the sample with lower density, the expansion height and

therefore the expansion time is higher. The small bubbles that are initially unobservable will continue to grow and thus be detectable.

It is important to note that the majority of the cells are reconstructed interconnected. The resolution is sufficient to reveal that the structure is predominantly with open cells.

The Figure 8 shows the anisotropy of the cells related to their height in the sample. It can be observed that, for this parameter, there is a difference between the upper and lower parts of the sample and the core. In the upper and lower parts the distribution seems to be linear, being more normally distributed in the core. To study the differences of the cells in the thickness, three study areas in the sub-volume were defined. The base and the top will correspond to the lower and upper 20 % of the sub-volume. The core will correspond to the rest. In this way, the study of the lower and upper layers, also known as skins or skin layers in the literature [46, 47, 48] , and their effects is studied. Thereafter the term "skin effect" will be used to describe the influence of the skin layer on the material properties. The difference between the base and the side where the expansion ends is also studied.

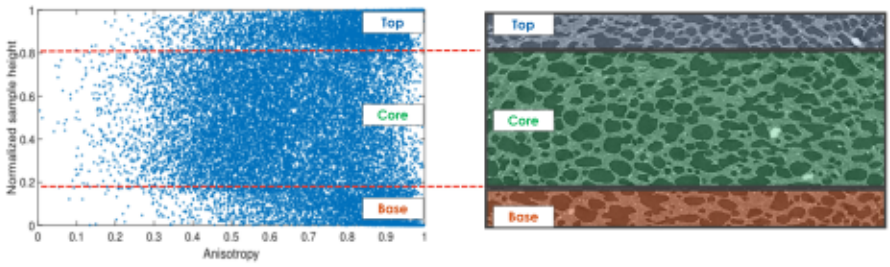


Figure 8: Relationship between sample height and anisotropy.

### *3.2. Cell size*

The length and width median values and first (Q1) and third (Q3) quartiles of the cells are presented in Table 1. In the core of the samples the cell sizes are comparable between the two samples. However, at the extremities, the cells are wider and longer.

| | Q1 length | Median length | Q3 length | Q1 width | Median width | Q3 widt |
|---|---|---|---|---|---|---|
| Low density | 164 $\mu m$ | 294 $\mu m$ | 520 $\mu m$ | 111 $\mu m$ | 176 $\mu m$ | 271 $\mu m$ |
| High density | 139 $\mu m$ | 262 $\mu m$ | 544 $\mu m$ | 88 $\mu m$ | 160 $\mu m$ | 278 $\mu m$ |

Table 1: Length and width statistic of the cells

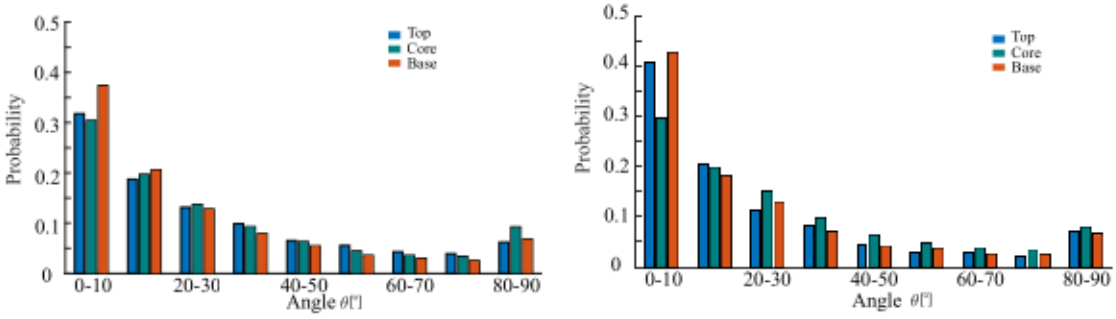


(a) Angle $\theta$ low density.

(b) Angle $\theta$ high density.

Figure 9: Comparison of the cells $\theta$-orientation for the two samples.

There are some large cells but a large majority (around 70 % of the cells) has a volume less than 0.01 $mm^3$. Of these, the majority have a volume inferior to 0.002 $mm^3$. There is no significant difference between core and skin.

### *3.3. Orientation of the cells*

The orientations according to the angle $\theta$ of the cells is represented in the Figure 9. The cells are mostly oriented with an angle $\theta$ close to 0° in both samples.

For the low density sample (Figure 9a), about 50 % of the cells are oriented with an angle lower than 20°. Variations are less than 5 % for all angles and for all three study areas. That means that the orientations are equivalent regardless of the area and the cells are directed perpendicular to the expansion.

For the high density sample (Figure 9b), about 50 % of the cells are oriented with an angle lower than 20° in the core area. In the extremities, about 50 % of the cells are oriented with an angle lower than 10°. That means that the cells are directed quite perpendicular to the expansion in all the sample but a skin is visible with a more pronounced phenomenon in the upper and lower extremities.

The study of the orientation with the $\phi$ angle presents equivalent results for both samples. About 40 % of the cells are oriented with an angle higher than 70° . There is a quite constant increase in the proportion of cells with increasing angle. For low angles the proportion is about 5 % up to about 20 % for the highest angles. This indicates that the majority of cells tends to be oriented in the XY plane.

### *3.4. Cell shape*

The anisotropy of the cells for both samples is represented in Figures 10a and 10b. Both samples show similar cell anisotropies. In the extremities one has less than 20 % of cells with anisotropy inferior to 0.5. There is then a

rapid, almost linear increase in proportion as a function of anisotropy (see in Figure 10b). In the core, however, a more harmonious distribution of cells between anisotropies of 0.3 and 1 is observed (see in Figure 10a).

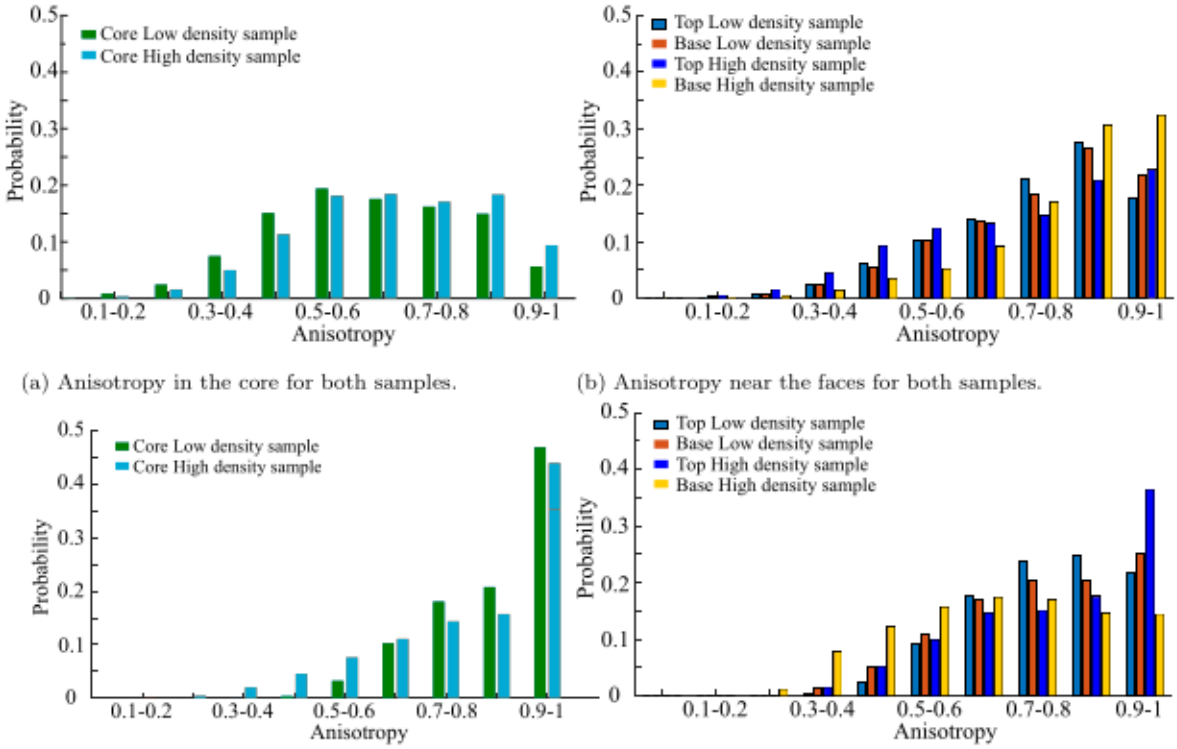


(a) Anisotropy in the core for both samples.

(b) Anisotropy near the faces for both samples.

(c) Sphericity in the core for both samples.

(d) Sphericity near the faces for both samples.

Figure 10: Anisotropy and sphericity comparison between core and extremities for both samples.

The sphericity of the cells for both samples is represented in Figures 10c and 10d . A difference of the cells sphericity between core and skin on the two samples is obvious.

It is remarkable that for both samples almost half (45 %) of the cells have a high sphericity superior to 0.9 in the core (see in Figure 10c) . The

distribution is much more heterogeneous in the skins (see in Figure 10d). For the low density sample, 80 % of cells have a sphericity greater than 0.7 in the core while this proportion drops to 65 % in the skin. For the high density sample 75 % of cells have a sphericity greater than 0.7 in the core while 50 (base) to 60 (top) % in the skin.

It has been shown that there is a difference in morphometric parameters between the cores of the samples and the extremities in contact with the metal plates covered with anti-adhesion paper. This skin layer exists for both sample types. Core cells have a less elongated shape, greater sphericity, and an orientation more perpendicular to the expansion than at the extremities. In all likelihood the boundary conditions during the foaming process influence the microstructure. Indeed, the gas is released into the soft material and disperses. It will be blocked by the metal plate on each side. Körner et al. [49] illustrated the developing of metallic foams within the constraints of walls. Nadella et al. used platen to block and heat a polymeric material to control the shape of the cells through the thickness and create a skin [50]. These two papers thus present results similar to those obtained for these TCSA materials confirming the hypothesis.

### *3.5. Strain field observed with DIC*

The Figure 11a shows the evolution of the shear strain field in the material during the test. The Figures b) to f) confirms that the field is quasi-homogeneous in the core of the sample throughout the test. The image correlation shows that at maximum the tensile strain $\epsilon_{yy}$ reaches a value of 0.0006 or 2.4% of the shear strain $\gamma$. The hypothesis of pure shear with small deformations is therefore assumed to be valid. Thus, the stress tensor $T$ is,

$$T = \begin{pmatrix} \sigma_1 & \tau & 0 \\ \tau & \sigma_2 & 0 \\ 0 & 0 & 0 \end{pmatrix} \overset{small\ strain}{\approx} \begin{pmatrix} 0 & \tau & 0 \\ \tau & 0 & 0 \\ 0 & 0 & 0 \end{pmatrix} \tag{3}$$

and the Green-Lagrange tensor $E$ is,

$$E = \begin{pmatrix} 0 & \gamma & 0 \\ \gamma & \gamma^2/2 & 0 \\ 0 & 0 & 0 \end{pmatrix} \overset{small\ strain}{\approx} \begin{pmatrix} 0 & \gamma & 0 \\ \gamma & 0 & 0 \\ 0 & 0 & 0 \end{pmatrix}. \tag{4}$$

The Figure 11b shows the evolution of the shear strain in the thickness along the line shown in the Figure 11a a). For this example, the sample thickness is 7 $mm$ and the position 0 is the middle of it. One observes a small asymmetry of the curve explainable by the movements of the adherends and has been seen with the DIC. One undergoes effort and movement and the other is fixed.

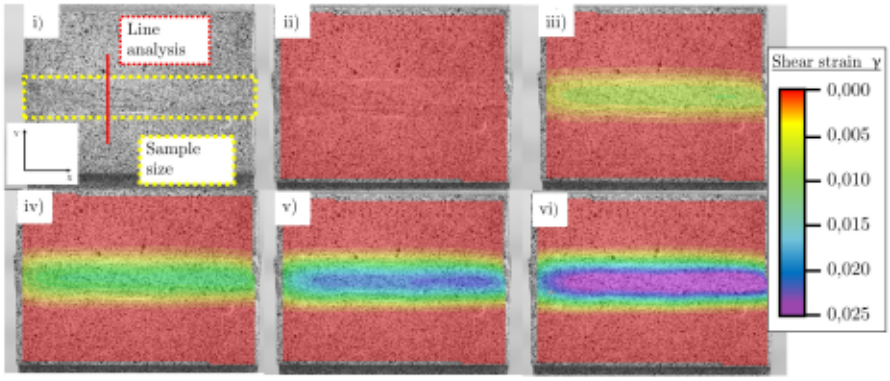


(a) Sample size on picture (i), and strain field during the test at loading = 0 % $F_{max}$ (ii), loading = 25 % $F_{max}$ (iii), loading = 50 % $F_{max}$ (iv), loading = 75 % $F_{max}$ (v), and before fracture (vi).

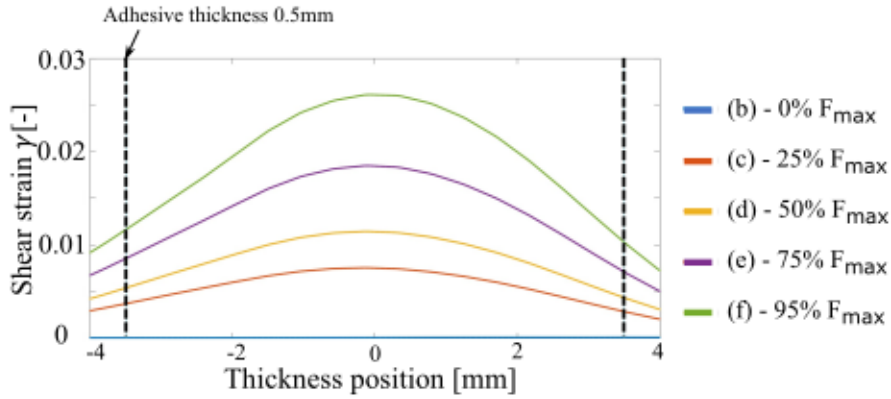


(b) Evolution of the shear strain along the thickness.

Figure 11: Analysis of the shear stress field during the test.

The bonding with epoxy adhesive is stiffer than the epoxy foam (but well below the aluminum)and can explain the strain gradient near the interface. When the glue was removed during the preparation of the samples, some of it may have remained on the substrate (as seen in Figure 2). On the tensile strain field in Figure 12 it seems that the red area fits the residual

glue location. This can explain the small shear strain in the substrates area.

Sample failure occurs cohesively in the core of the sample, always on the side of the effort. These results validate the use of this method to characterize the mechanical properties of this type of material.

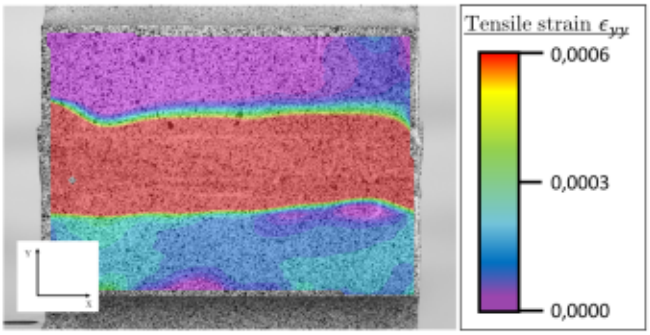


Figure 12: Tensile strain field at the end of the test.

### *3.6. Influence of density on stress*

Figure 13 shows the results curves of the shear tests for the samples of the two different thicknesses and density.

One can observe a first part of the curve approximately linear until 50% of the maximum loading. Then, a non-linearity implies a change in behavior. After reaching a maximum stress the sample breaks in a brittle way. The image acquisition frequency does not allow to study the behavior after the maximum effort, explaining the sudden end of the curve. The last point of the curve corresponds to the last moment before a fall to zero of the force, not represented in the figure for reasons of readability.

It is known in the literature that thermosetting polymers like epoxy have low viscosity [51] allowing to put aside viscosity effects for the curve slope softening. Heterogeneous quasi-brittle materials such as concrete [52] are

known to be damaged with a stable propagation of micro cracks before an unstable propagation of cracks until macro failure. It is assumed that this variation is due to the presence of micro-damages of the material. More local observation like in-situ tests under tomography might confirm it. Fracture tests with compact tension samples for example could to confirm the quasi-brittle behavior of this material.

One can therefore affirm the quasi-brittle behavior of this material. The average maximum shear strain and standard deviation are presented in the Table 2 as well as the shear modulus (normalized by a fixed value) and its variation.

| | Average max shear strain | Standard deviation | Average normalized shear modulus | Modulus variation |
|---|---|---|---|---|
| low density | 0.023 | 0.003 | 23.8 | ±10 % |
| high density | 0.029 | 0.007 | 32.2 | ±11 % |

Table 2: Mechanical properties comparison between low and high density samples.

The elastic modulus is 26 % lower for the sample with the lowest density. The average maximum shear strain is also different between the two types of samples. The denser samples have on average a 26 % larger maximum shear strain. However, the average maximum stress is comparable between both samples series. The difference between the two mean values is smaller than the standard deviation of each series. That means that the driving factor is the stress.

### *3.7. Foam-like behavior*

In the Figure 13 one could observe a difference in shear behavior for both types of samples. There is however a difference in density between the two. The tomography allowed to show that the structure looks like an open cell

foam. Gibson and Ashby [26] show with a micromechanical model that the shear modulus $G*$ (and thus the stress) is related to $(\rho^*)^2$ by the relation :

$$\frac{G^*}{E_s} = C_2 \left(\frac{\rho^*}{\rho_s}\right)^2 \tag{5}$$

For these samples $E_s$ and $\rho_s$ are constant and identical for both types of samples. The shear stress values from Figure 13 were thus divided by the density according to eq. 5 (see in Figure 14). Discrepancies between the two densities are largely reduced.

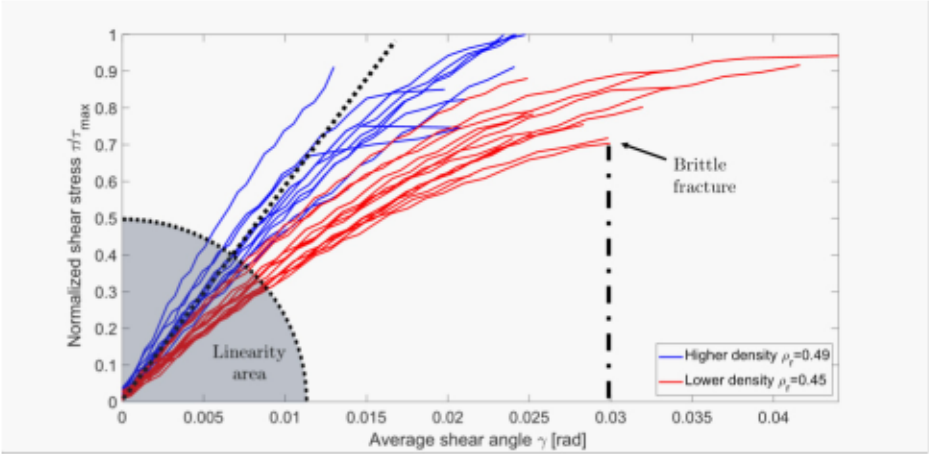


Figure 13: Stress-strain Arcan curves for both types of samples.

It appears that the shear modulus of such cellular structual adhesive is mainly governed by the density and can be determined with the eq. 5 proposed by Gibson and Ashby. It is interesting to note that the microstructure variations between low and high density do not influence significantly the result. The macroscopic density factor is sufficient to describe the variations of the results.

Furthermore, the maximum shear strain is, on average, related to the density of the samples on the same order of magnitude as the shear modulus. The increase in porosity will therefore make the material softer.

It would appear that material failure is not directly related to macroscopic density. There are probably micro-cracks in the material and the complex structure will determine how the material will fail.

The use of a model based on micromechanics at the cellular scale thus seems to be a relevant first approximation to describe the macroscopic behavior of the material. The material failure being however not explained by this model, a study of the behavior of the material at the cellular scale is necessary. In-situ testing under X-ray microtomography could provide answers to these questions.

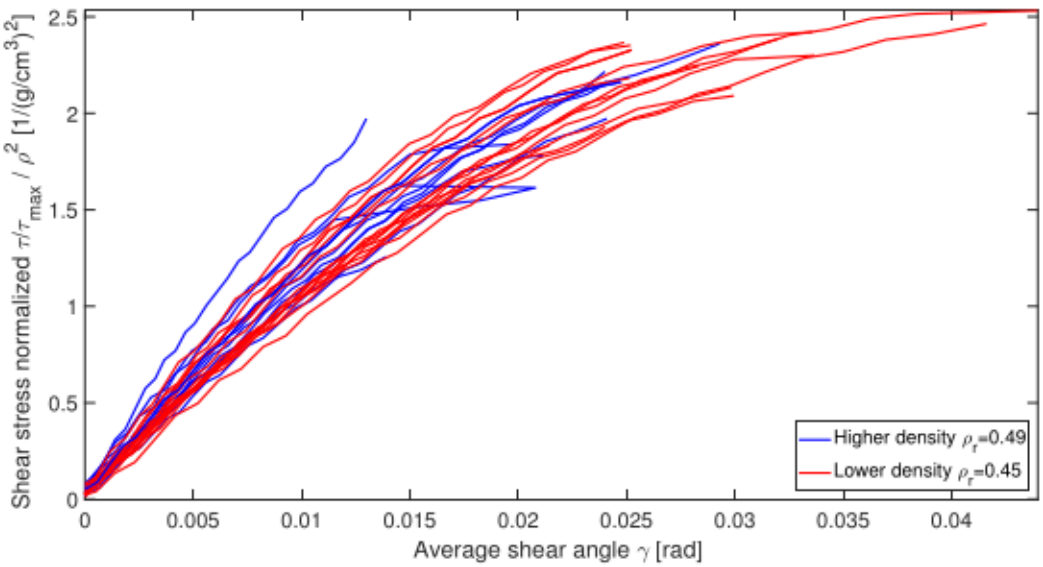


Figure 14: Stress-strain Arcan curves normalized by squared density.

## 4. Conclusion

In the present study, the behaviour of TCSA under shear loading was studied. It was shown the existence of a skin layer in the TCSA open-cell microstructure due to the foaming process. The cells were observed to be more spherical in the core of the material whereas they becomes elongated close to the upper and lower faces. Samples with different densities display similar microstructure.

The Arcan shear test allowed to determine the mechanical properties of the material and its behavior under shear loading. The homogeneity of the strain field through the test was verified thanks to DIC method. The skin effect does not seem to be the most relevant parameter influencing the macroscopic elastic mechanical properties of the material. It was shown that using the relation linking the shear modulus to the density squared, proposed by Gibson and Ashby, is a first approximation, at this scale, to predict the macroscopic shear modulus and the maximum shear strain at failure of TCSA which is not the case for the maximum shear stress at failure. More local measurements and observations would be needed in order to link the heterogeneous microstructure and the fracture properties. Moreover the adhesive properties of cellular structural adhesive could also be of interest.

## References

[1] J. Cognard, Science et technologie du collage, Presses Polytechniques et Universitaires Romandes, Lausanne, 2004. OCLC: 932532694.

[2] C. S. Adderley, Adhesive Bonding, Materials & Design 9 (1988) 287–

293. URL: https://www.sciencedirect.com/science/article/pii/0261306988900064. doi:10.1016/0261-3069(88)90006-4.

[3] D14 Committee, Test Method for Thick-Adherend Metal Lap-Shear Joints for Determination of the Stress-Strain Behavior of Adhesives in Shear by Tension Loading, Technical Report, ASTM International, ????. URL: http://www.astm.org/cgi-bin/resolver.cgi?D5656-10R17. doi:10.1520/D5656-10R17.

[4] D14 Committee, Test Method for Apparent Shear Strength of Single-Lap-Joint Adhesively Bonded Metal Specimens by Tension Loading (Metal-to-Metal), Technical Report, ASTM International, ????. URL: http://www.astm.org/cgi-bin/resolver.cgi?D1002-10R19. doi:10.1520/D1002-10R19.

[5] L. Liao, C. Huang, T. Sawa, Effect of adhesive thickness, adhesive type and scarf angle on the mechanical properties of scarf adhesive joints, International Journal of Solids and Structures 50 (2013) 4333–4340. URL: https://www.sciencedirect.com/science/article/pii/S0020768313003521. doi:10.1016/j.ijsolstr.2013.09.005.

[6] M. Arcan, Z. Hashin, A. Voloshin, A method to produce uniform plane-stress states with applications to fiber-reinforced materials: A specially designed specimen yields material properties under pure shear or uniform plane-stress conditions, Experimental Mechanics 18 (1978) 141–146. URL: http://link.springer.com/10.1007/BF02324146. doi:10.1007/BF02324146.

[7] A. Jouan, A. Constantinescu, A critical comparison of shear tests for adhesive joints, International Journal of Adhesion and Adhesives 84 (2018) 63–79. URL: https://linkinghub.elsevier.com/retrieve/pii/S0143749618300745. doi:10.1016/j.ijadhadh.2018.02.035.

[8] J. Cognard, R. Créac'hcadec, L. Sohier, P. Davies, Analysis of the nonlinear behavior of adhesives in bonded assemblies—Comparison of TAST and Arcan tests, International Journal of Adhesion and Adhesives 28 (2008) 393–404. URL: https://linkinghub.elsevier.com/retrieve/pii/S0143749608000390. doi:10.1016/j.ijadhadh.2008.04.006.

[9] J. Xavier, J. Morais, F. Pereira, Non-linear shear behaviour of bovine cortical bone by coupling the Arcan test with digital image correlation, Optics and Lasers in Engineering 110 (2018) 462–470. URL: https://linkinghub.elsevier.com/retrieve/pii/S0143816618302288. doi:10.1016/j.optlaseng.2018.07.004.

[10] P. Bilko, A. Skoratko, A. Rutkiewicz, L. Małyszko, Determination of the Shear Modulus of Pine Wood with the Arcan Test and Digital Image Correlation, Materials 14 (2021) 468. URL: https://www.mdpi.com/1996-1944/14/2/468. doi:10.3390/ma14020468.

[11] L. Alfonso, C. Badulescu, N. Carrere, Use of the modified Arcan fixture to study the strength of bonded assemblies for automotive applications, International Journal of Adhesion and Adhesives 80 (2018) 104–114. URL: https://linkinghub.elsevier.com/retrieve/pii/S0143749617301744. doi:10.1016/j.ijadhadh.2017.09.014.

[12] N. Burst, D. O. Adams, H. E. Gascoigne, Investigating the Thin-Film Versus Bulk Material Properties of Structural Adhesives, The Journal of Adhesion 87 (2011) 72–92. URL: http://www.tandfonline.com/doi/abs/10.1080/00218464.2011.538326. doi:10.1080/00218464.2011.538326.

[13] A. A. Taib, R. Boukhili, S. Achiou, S. Gordon, H. Boukehili, Bonded joints with composite adherends. Part I. Effect of specimen configuration, adhesive thickness, spew fillet and adherend stiffness on fracture, International Journal of Adhesion and Adhesives 26 (2006) 226–236. URL: https://linkinghub.elsevier.com/retrieve/pii/S0143749605000539. doi:10.1016/j.ijadhadh.2005.03.015.

[14] L. Grant, R. Adams, L. F. da Silva, Experimental and numerical analysis of single-lap joints for the automotive industry, International Journal of Adhesion and Adhesives 29 (2009) 405–413. URL: https://linkinghub.elsevier.com/retrieve/pii/S0143749608000985. doi:10.1016/j.ijadhadh.2008.09.001.

[15] P. Davies, L. Sohier, J.-Y. Cognard, A. Bourmaud, D. Choqueuse, E. Rinnert, R. Créac'hcadec, Influence of adhesive bond line thickness on joint strength, International Journal of Adhesion and Adhesives 29 (2009) 724–736. URL: https://linkinghub.elsevier.com/retrieve/pii/S0143749609000402. doi:10.1016/j.ijadhadh.2009.03.002.

[16] P. Zuo, A. P. Vassilopoulos, Review of fatigue of bulk structural adhesives and thick adhesive joints, International Materials Reviews

66 (2021) 313–338. URL: https://doi.org/10.1080/09506608.2020.1845110. doi:10.1080/09506608.2020.1845110, publisher: Taylor & Francis _eprint: https://doi.org/10.1080/09506608.2020.1845110.

[17] R. Lopes Fernandes, S. Teixeira de Freitas, M. K. Budzik, J. A. Poulis, R. Benedictus, From thin to extra-thick adhesive layer thicknesses: Fracture of bonded joints under mode I loading conditions, Engineering Fracture Mechanics 218 (2019) 106607. URL: https://linkinghub.elsevier.com/retrieve/pii/S0013794419300852. doi:10.1016/j.engfracmech.2019.106607.

[18] F. Delzendehrooy, A. Akhavan-Safar, A. Q. Barbosa, R. Beygi, D. Cardoso, R. J. C. Carbas, E. A. S. Marques, L. F. M. da Silva, A comprehensive review on structural joining techniques in the marine industry, Composite Structures 289 (2022) 115490. URL: https://www.sciencedirect.com/science/article/pii/S0263822322002811. doi:10.1016/j.compstruct.2022.115490.

[19] A. Wilson, Vehicle weight is the key driver for automotive composites, Reinforced Plastics 61 (2017) 100–102. URL: https://linkinghub.elsevier.com/retrieve/pii/S0034361715007006. doi:10.1016/j.repl.2015.10.002.

[20] J. Hoge, C. Leach, Epoxy resin infused boat hulls, Reinforced Plastics 60 (2016) 221–223. URL: https://www.sciencedirect.com/science/article/pii/S0034361716000187. doi:10.1016/j.repl.2016.01.002.

[21] Y. Ding, M. H. Hassan, O. Bakker, S. Hinduja, P. Bártolo, A Review on Microcellular Injection Moulding, Materials 14 (2021) 4209. URL: https://www.mdpi.com/1996-1944/14/15/4209. doi:10.3390/ma14154209, number: 15 Publisher: Multidisciplinary Digital Publishing Institute.

[22] G. J. Davies, S. Zhen, Metallic foams: their production, properties and applications, Journal of Materials Science 18 (1983) 1899–1911. URL: http://link.springer.com/10.1007/BF00554981. doi:10.1007/BF00554981.

[23] L. J. Gibson, Mechanical Behavior of Metallic Foams, Annual Review of Materials Science 30 (2000) 191–227. URL: https://www.annualreviews.org/doi/10.1146/annurev.matsci.30.1.191. doi:10.1146/annurev.matsci.30.1.191.

[24] A. Siegmann, S. Kenig, D. Alperstein, M. Narkis, Mechanical behavior of reinforced polyurethane foams, Polymer Composites 4 (1983) 113–119. URL: http://onlinelibrary.wiley.com/doi/abs/10.1002/pc.750040206. doi:10.1002/pc.750040206, _eprint: https://onlinelibrary.wiley.com/doi/pdf/10.1002/pc.750040206.

[25] E. H. Kerner, The Elastic and Thermo-elastic Properties of Composite Media, Proceedings of the Physical Society. Section B 69 (1956) 808–813. URL: https://doi.org/10.1088/0370-1301/69/8/305. doi:10.1088/0370-1301/69/8/305, publisher: IOP Publishing.

[26] L. J. Gibson, M. F. Ashby, Cellular Solids: Structure and Properties, 2

ed., Cambridge University Press, 1997. URL: https://www.cambridge.org/core/product/identifier/9781139878326/type/book. doi:10.1017/CBO9781139878326.

[27] F. Saint-Michel, L. Chazeau, J.-Y. Cavaillé, E. Chabert, Mechanical properties of high density polyurethane foams: I. Effect of the density, Composites Science and Technology 66 (2006) 2700–2708. URL: https://www.sciencedirect.com/science/article/pii/S0266353806001114. doi:10.1016/j.compscitech.2006.03.009.

[28] R. M. Christensen, Mechanics of low density materials, Journal of the Mechanics and Physics of Solids 34 (1986) 563–578. URL: https://www.sciencedirect.com/science/article/pii/0022509686900372. doi:10.1016/0022-5096(86)90037-2.

[29] P. Viot, D. Bernard, Multi-scale foam behaviour characterisation, in: Computational Methods and Experiments in Materials Characterisation III, volume I, WIT Press, Bologna, Italy, 2007, pp. 197–206. URL: http://library.witpress.com/viewpaper.asp?pcode=MC07-020-1. doi:10.2495/MC070201, iSSN: 1743-3533, 1746-4471.

[30] P. Viot, F. Beani, J.-L. Lataillade, Polymeric foam behavior under dynamic compressive loading, Journal of Materials Science 40 (2005) 5829–5837. URL: https://doi.org/10.1007/s10853-005-4998-5. doi:10.1007/s10853-005-4998-5.

[31] R. Bouix, P. Viot, J.-L. Lataillade, Polypropylene foam behaviour

under dynamic loadings: Strain rate, density and microstructure effects, International Journal of Impact Engineering 36 (2009) 329–342. URL: https://www.sciencedirect.com/science/article/pii/S0734743X08000791. doi:10.1016/j.ijimpeng.2007.11.007.

[32] L. Marșavina, E. Linul, Fracture toughness of rigid polymeric foams: A review, Fatigue & Fracture of Engineering Materials & Structures 43 (2020) 2483–2514. URL: http://onlinelibrary.wiley.com/doi/abs/10.1111/ffe.13327. doi:10.1111/ffe.13327, _eprint: https://onlinelibrary.wiley.com/doi/pdf/10.1111/ffe.13327.

[33] G. Dong, G. Zhao, Y. Guan, G. Wang, X. Wang, The cell forming process of microcellular injection-molded parts, Journal of Applied Polymer Science 131 (2014). URL: https://onlinelibrary.wiley.com/doi/abs/10.1002/app.40365. doi:10.1002/app.40365, _eprint: https://onlinelibrary.wiley.com/doi/pdf/10.1002/app.40365.

[34] J. Gómez-Monterde, M. Schulte, S. Ilijevic, J. Hain, M. Sánchez-Soto, O. O. Santana, M. L. Maspoch, Effect of microcellular foaming on the fracture behavior of ABS polymer, Journal of Applied Polymer Science 133 (2016). URL: http://onlinelibrary.wiley.com/doi/abs/10.1002/app.43010. doi:10.1002/app.43010, _eprint: https://onlinelibrary.wiley.com/doi/pdf/10.1002/app.43010.

[35] X. Huo, Z. Jiang, Q. Luo, Q. Li, G. Sun, Mechanical characterization and numerical modeling on the yield and fracture behaviors of polymethacrylimide (PMI) foam materials, International Journal of Mechanical Sciences 218 (2022)

107033. URL: https://linkinghub.elsevier.com/retrieve/pii/S0020740321007013. doi:10.1016/j.ijmecsci.2021.107033.

[36] S. Taher, O. Thomsen, J. Dulieu-Barton, S. Zhang, Determination of mechanical properties of PVC foam using a modified Arcan fixture, Composites Part A: Applied Science and Manufacturing 43 (2012) 1698–1708. URL: https://linkinghub.elsevier.com/retrieve/pii/S1359835X11003812. doi:10.1016/j.compositesa.2011.11.010.

[37] E. Maire, J. Y. Buffière, L. Salvo, J. J. Blandin, W. Ludwig, J. M. Létang, On the Application of X-ray Microtomography in the Field of Materials Science, Advanced Engineering Materials 3 (2001) 539. URL: https://onlinelibrary.wiley.com/doi/10.1002/1527-2648(200108)3:8<539::AID-ADEM539>3.0.CO;2-6. doi:10.1002/1527-2648(200108)3:8<539::AID-ADEM539>3.0.CO;2-6.

[38] T. Dillard, F. N'guyen, E. Maire, L. Salvo, S. Forest *, Y. Bienvenu, J.-D. Bartout, M. Croset, R. Dendievel, P. Cloetens, 3D quantitative image analysis of open-cell nickel foams under tension and compression loading using X-ray microtomography, Philosophical Magazine 85 (2005) 2147–2175. URL: http://www.tandfonline.com/doi/abs/10.1080/14786430412331331916. doi:10.1080/14786430412331331916.

[39] L. Le Barbenchon, J. Girardot, J.-B. Kopp, P. Viot, Multi-scale foam : 3D structure/compressive behaviour relationship of agglomerated cork, Materialia 5 (2019) 100219. URL: https://linkinghub.elsevier.

com/retrieve/pii/S2589152919300146. doi:10.1016/j.mtla.2019.100219.

[40] O. Olurin, M. Arnold, C. Körner, R. Singer, The investigation of morphometric parameters of aluminium foams using micro-computed tomography, Materials Science and Engineering: A 328 (2002) 334–343. URL: https://linkinghub.elsevier.com/retrieve/pii/S0921509301018093. doi:10.1016/S0921-5093(01)01809-3.

[41] Y. Liu, Z. Zhang, X. Liu, L. Wang, X. Xia, Efficient image segmentation based on deep learning for mineral image classification, Advanced Powder Technology 32 (2021) 3885–3903. URL: https://linkinghub.elsevier.com/retrieve/pii/S092188312100412X. doi:10.1016/j.apt.2021.08.038.

[42] H. G. Merkus, Particle Size, Size Distributions and Shape, in: H. G. Merkus (Ed.), Particle Size Measurements: Fundamentals, Practice, Quality, Springer Netherlands, Dordrecht, 2009, pp. 13–42. URL: https://doi.org/10.1007/978-1-4020-9016-5_2. doi:10.1007/978-1-4020-9016-5_2.

[43] S. Yoneyama, Basic principle of digital image correlation for in-plane displacement and strain measurement, Advanced Composite Materials 25 (2016) 105–123. URL: https://doi.org/10.1080/09243046.2015.1129681. doi:10.1080/09243046.2015.1129681, publisher: Taylor & Francis _eprint: https://doi.org/10.1080/09243046.2015.1129681.

[44] J. Liu, D. Saletti, S. Pattofatto, H. Zhao, Impact testing of poly-

meric foam using Hopkinson bars and digital image analysis, Polymer Testing 36 (2014) 101–109. URL: https://linkinghub.elsevier.com/retrieve/pii/S0142941814000725. doi:10.1016/j.polymertesting.2014.03.014.

[45] S. Roux, F. Hild, P. Viot, D. Bernard, Three-dimensional image correlation from X-ray computed tomography of solid foam, Composites Part A: Applied Science and Manufacturing 39 (2008) 1253–1265. URL: https://linkinghub.elsevier.com/retrieve/pii/S1359835X07002606. doi:10.1016/j.compositesa.2007.11.011.

[46] J. Banhart, J. Baumeister, Deformation characteristics of metal foams, Journal of Materials Science 33 (1998) 1431–1440. URL: http://link.springer.com/10.1023/A:1004383222228. doi:10.1023/A:1004383222228.

[47] M. R. Barzegari, D. Rodrigue, The effect of injection molding conditions on the morphology of polymer structural foams, Polymer Engineering & Science 49 (2009) 949–959. URL: http://onlinelibrary.wiley.com/doi/abs/10.1002/pen.21283. doi:10.1002/pen.21283, _eprint: https://onlinelibrary.wiley.com/doi/pdf/10.1002/pen.21283.

[48] M.-C. D. Jawhar, D. Blanc, P. Chaumont, P. Cassagnau, Study of the Coalescence Mechanisms During Silicone Foaming, Macromolecular Materials and Engineering 299 (2014) 336–343. URL: http://onlinelibrary.wiley.com/doi/abs/10.1002/mame.201300142. doi:10.1002/mame.201300142, _eprint: https://onlinelibrary.wiley.com/doi/pdf/10.1002/mame.201300142.

[49] C. Körner, M. Thies, R. Singer, Modeling of Metal Foaming with Lattice Boltzmann Automata, Advanced Engineering Materials 4 (2002) 765–769. URL: http://onlinelibrary.wiley.com/doi/abs/10.1002/1527-2648%2820021014%294%3A10%3C765%3A%3AAID-ADEM765%3E3.0.CO%3B2-M. doi:10.1002/1527-2648(20021014)4:10<765::AID-ADEM765>3.0.CO;2-M, _eprint: https://onlinelibrary.wiley.com/doi/pdf/10.1002/1527-2648%2820021014%294%3A10%3C765%3A%3AAID-ADEM765%3E3.0.CO%3B2-M.

[50] K. Nadella, V. Kumar, W. Li, Constrained Solid-State Foaming of Microcellular Panels, Cellular Polymers 24 (2005) 71–90. URL: http://journals.sagepub.com/doi/10.1177/026248930502400202. doi:10.1177/026248930502400202.

[51] M. J. Mullins, D. Liu, H. J. Sue, 2 - Mechanical properties of thermosets, in: Q. Guo (Ed.), Thermosets, Woodhead Publishing, 2012, pp. 28–61. URL: https://www.sciencedirect.com/science/article/pii/B978085709086750002X. doi:10.1533/9780857097637.1.28.

[52] Y. Li, D. Jia, Z. Rui, J. Peng, C. Fu, J. Zhang, Evaluation method of rock brittleness based on statistical constitutive relations for rock damage, Journal of Petroleum Science and Engineering 153 (2017) 123–132. URL: https://linkinghub.elsevier.com/retrieve/pii/S0920410517303947. doi:10.1016/j.petrol.2017.03.041.